Spherical momentum distribution of the protons in hexagonal ice from modeling of inelastic neutron scattering data

D. Flammini, A. Pietropaolo, R. Senesi, C. Andreani, F. McBride et al.

Related Articles

Adiabatic and non-adiabatic quantum dynamics calculation of O(1D) + D2 OD + D reaction
J. Chem. Phys. 135, 234301 (2011)

New ab initio coupled potential energy surfaces for the Br(2P3/2, 2P1/2) + H2 reaction
J. Chem. Phys. 135, 164311 (2011)

Reaction between graphene and hydrogen under oblique injection
J. Appl. Phys. 110, 084320 (2011)

An experimental and computational study of the reaction of ground-state sulfur atoms with carbon disulfide
J. Chem. Phys. 135, 144306 (2011)

The dissociative chemisorption of methane on Ni(100): Reaction path description of mode-selective chemistry
J. Chem. Phys. 135, 114701 (2011)

Additional information on J. Chem. Phys.

Spherical momentum distribution of the protons in hexagonal ice from modeling of inelastic neutron scattering data

D. Flammini,[1] A. Pietropaolo,[1] R. Senesi,[1,a)] C. Andreani,[1] F. McBride,[2] A. Hodgson,[2] M. A. Adams,[3] L. Lin,[4] and R. Car[5]

[1]*Università degli Studi di Roma "Tor Vergata," Dipartimento di Fisica and Centro NAST, Via della Ricerca Scientifica 1, 00133 Roma, Italy*
[2]*Department of Chemistry, Surface Science Research Centre, University of Liverpool, United Kingdom*
[3]*STFC Rutherford Appleton Laboratory, ISIS Facility, Harwell Oxford, Didcot OX11 0QX, United Kingdom*
[4]*Program in Applied and Computational Mathematics, Princeton University Princeton, New Jersey 08544, USA*
[5]*Department of Chemistry and Department of Physics, Princeton University Princeton, New Jersey 08544, USA*

The spherical momentum distribution of the protons in ice is extracted from a high resolution deep inelastic neutron scattering experiment. Following a recent path integral Car-Parrinello molecular dynamics study, data were successfully interpreted in terms of an anisotropic Gaussian model, with a statistical accuracy comparable to that of the model independent scheme used previously, but providing more detailed information on the three dimensional potential energy surface experienced by the proton. A recently proposed theoretical concept is also employed to directly calculate the mean force from the experimental neutron Compton profile, and to evaluate the accuracy required to unambiguously resolve and extract the effective proton potential from the experimental data. © *2012 American Institute of Physics*. [doi:10.1063/1.3675838]

I. INTRODUCTION

Although liquid and solid phases of water are the focus of a considerable number of experimental and theoretical investigations because of their biological and technological importance,[1,2] several physical properties of water are not well understood. Progress in this area requires an accurate description of the proton motion in hydrogen bonded systems, something that has been difficult to measure directly. Recently new experimental and simulation techniques have been used to probe the quantum state of protons in water and ice by examining the proton momentum distribution, $n(p)$, which is mainly determined by quantum effects.[3] Experimentally, $n(p)$ can be directly measured by deep inelastic neutron scattering (DINS),[4–6] where neutrons probe proton dynamics at high energy, $\hbar\omega$, and high momentum, $\hbar q$, transfers. As well as providing information on proton quantum dynamics, DINS is also sensitive to the proton's local environment, i.e., the potential of mean force experienced by the protons. In recent years, several DINS experiments have addressed the study of bulk water in stable liquid,[7] solid,[8] and supercooled liquid[13,14] phases and in confined geometry.[15–18] In parallel, novel simulation techniques have been employed to calculate the $n(p)$ using open path integral simulations[19] implemented with first principles molecular dynamics[20] within the path integral Car-Parrinello molecular dynamics (PICPMD) framework.[21] The path integral simulation has access to the three dimensional $n(\vec{p})$, and thus provides complementary information to the spherically averaged $n(p)$ obtained via DINS

from isotropic ice. The calculated $n(p)$ in ice from Ref. 19 revealed good overall agreement but also some discrepancies with previous DINS measurements on ice at T=269 K by Reiter *et al.*[8] In particular, the calculated $n(p)$ had more weight at large momenta and a more extended tail than in the experiment, indicating that in the simulation the proton was spatially more localized and hence had a larger kinetic energy than in the experiment. This is a somewhat surprising result, given that the main physical approximation in the PICPMD simulation is in the exchange-correlation functional and the approximations commonly adopted for this functional are expected to favor proton delocalization over localization.[9] This paper reports new theoretical analysis and interpretation of PICPMD simulations on ice at 269 K and a high resolution DINS experiment on ice at 271 K. At these temperatures, $n(p)$ in ice is due almost entirely to zero point motion, providing a sensitive probe of the proton's local environment. We stress that the DINS experiments give a direct access to the zero-point kinetic energy of the proton, while the estimates of the proton kinetic energy from a combination of optical and inelastic neutron scattering results assume an harmonic approximation and decoupling between the degrees of freedom of translation, rotation (libration), and internal vibrations.[10,11] In the case of hydrogen-bonded systems, these assumptions are more appropriate for isolated molecules such as in the dilute vapour phase, while in the condensed phases one would expect the decoupling of degrees of freedom, as well as a fully harmonic description not to hold anymore.[10,11]

Indeed it was found, in Ref. 12, that the momentum distribution in ice at 269 K was better described by a quasi-harmonic than by a fully harmonic model, whereas in the

---

supercooled liquid at 271 K the large excess of the proton mean kinetic energy was interpreted, in Ref. 13, in terms of a very substantial anharmonicity of the potential energy surface.

Here we used refined DINS measurements, using resonance-detector (RD) and foil-cycling techniques (FCT),[22–24] providing remarkable improvements, with respect to existing measurements on bulk ice,[8] in both energy resolution (32% narrowing of FWHM), counting statistics, (1% error at the center of the overall neutron Compton profile (NCP) and of 15% at 1/15 of the peak height, respectively), and a much better separation between proton and heavy atoms peaks in the sample and the container. The latter eliminates any possible spurious distortion due to inaccurate subtraction of the O, Al contributions.[25] The uncertainty in the determined mean kinetic energy, $\langle E_K \rangle$, 11% in the previous measurements,[8] is $\simeq 2\%$ in the present case. Moreover, the current resolution line shape has a finite variance, allowing us also to carry out non parametric determinations of $\langle E_K \rangle$ as outlined below. DINS data were analyzed within the impulse approximation (IA),[26] i.e., a neutron-single atom scattering process with conservation of momentum and kinetic energy. The recoil energy is $\hbar \omega_r = \hbar^2 q^2 / 2M$, where M is the proton mass, and q is the wave vector transfer. The dynamical structure factor for an isotropic system is related to $n(p)$ by

$$S(q,\omega) = \int n(p)\delta\left(\omega - \frac{\hbar q^2}{2M} - \frac{\mathbf{q} \cdot \mathbf{p}}{M}\right)dp = \frac{M}{q} J_{IA}(y),$$
(1)

where $y = \frac{M}{q}(\omega - \frac{\hbar q^2}{2M})$,[26] $J_{IA}(y)$ is the longitudinal $n(p)$, or neutron Compton profile, and $\langle E_K \rangle = \frac{3\hbar^2}{2M}\int_{-\infty}^{\infty} y^2 J_{IA}(y)dy = \frac{3\hbar^2}{2M}\sigma^2$. For an isotropic system

$$J_{IA}(y) = 2\pi\hbar \int_{|\hbar y|}^{\infty} p\, n(p)\, dp\ .$$
(2)

Within the IA framework, $J_{IA}(y)$ is symmetric and centred at $y = 0$ and related to $n(p)$ via:[3]

$$n(p) = -\frac{1}{2\pi\hbar^3 y}\left[\frac{dJ_{IA}(y)}{dy}\right]_{\hbar y = p}\ .$$
(3)

Four independent schemes, two non-parametric, and two parametric (fitting), were used in the analysis of the experimental data, in order to access $\langle E_K \rangle$, $n(p)$, and the proton mean force, using specifically developed methods. The results obtained show a complete consistency between the four independent schemes used in the analysis, assessing the reliability of the experimental data and the robustness of the physical interpretation, unprecedented for DINS experiments. These allow us to successfully extract the dominant features of the microscopic directional momentum distribution from an experiment on a macroscopically isotropic sample.

II. EXPERIMENT

The DINS experiment was performed at the time of flight VESUVIO spectrometer (ISIS neutron source-UK)[4] in the range $2.5\,\mathrm{eV} \leq \hbar\omega_r \leq 30\,\mathrm{eV}$. Scattered neutrons were detected by 64 scintillators,[27] in the angular range $32.75° \leq \vartheta \leq 72.5°$, for an integrated proton current $I_p = 3600\ \mu\mathrm{A}$ h. The sample was a $65 \times 65 \times 1\ \mathrm{mm}^3$ slab of polycrystalline ice contained in an Al holder, equipped with Rh/Fe thermometers. The sample was kept at a constant temperature, T=271.00 $\pm$ 0.01 K. At each scattering angle the energy of the scattered neutrons, E_1, is selected by using the RD and FCT by Au analyzers (E_1 = 4897 meV), providing a resolution in y-space of $\simeq 2$ Å^{-1} FWHM, and a complete removal of the sample-independent background.[28]

A. Data reduction

The Foil cycling technique provides the conversion of neutrons with final energy E_1 into prompt-γ photons that are detected using cerium-doped yttrium aluminium perovskite detectors.[27] Scattered neutrons are recorded as a function of their time of flight from the source to the detectors, and the kinematics of the scattering event is reconstructed according to the expression $t = t_0 + \frac{L_0}{v_0} + \frac{L_1}{v_1}$ where t_0 is a fixed electronic time delay, L_0 and L_1 are the (known) incident and scattering flight paths of the instrument, while v_0 and v_1 are the initial and final neutron velocities, respectively. Data reduction is carried out, using standard and *ad hoc* routines, to convert the observed count rate at each detector into the experimental neutron Compton profiles, for each detector. A "difference spectrum" is calculated using the Foil Cycling Technique. Each time of flight count rate spectrum, at a fixed detector, is determined by the difference between two "raw" time of flight spectra, one with the cycling foil between sample and detector, and one without the cycling foil between the sample and detector, as shown, for example, in Fig. 1. Data have been divided by the integrated counts measured from the incident neutron monitor. The signal is then
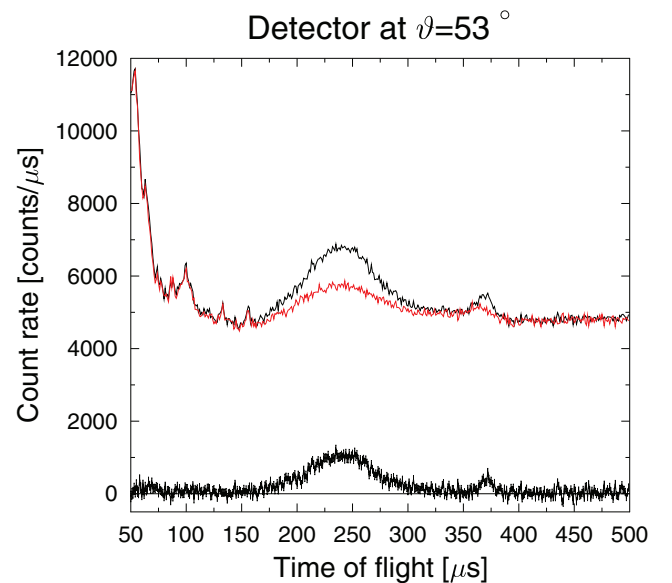

FIG. 1. Time of flight DINS signal from the ice sample, for $\vartheta \simeq 53°$. Red continuous line is the raw "foil out" spectrum, black continuous line is the raw "foil in" spectrum. Time of flight spectrum is reported as black markers with error bars. Proton recoil peak is centred at $t \simeq 240\ \mu$s, recoil peaks from oxygen and aluminium from the container are centred at $t \simeq 360\ \mu$s.
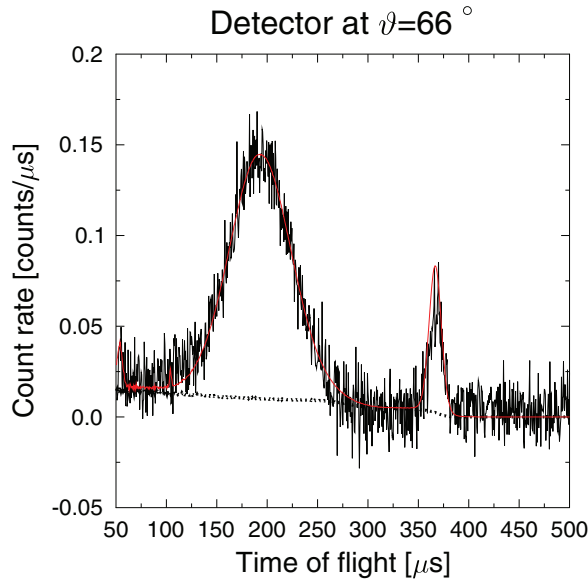
FIG. 2. Example of time of flight DINS experimental and simulated signals for a detector located at $\vartheta \simeq 66°$. The continuous line is the experimental spectrum (counting errors omitted); the red continuous line shows the MC simulations, with all scattering orders included, and the dashed line is the MC simulations with multiply scattered neutrons only, up to 5th order scattering.
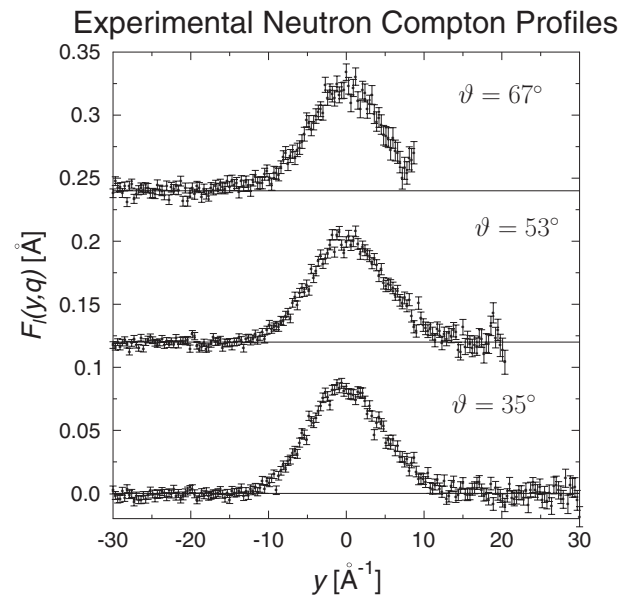

FIG. 3. Example of normalized $F_l(y, q)$ (markers with error bars), for three scattering angles. Two of the spectra are shifted upwards for clarity. For the two highest angles, the artificially imposed $F_l(y, q) = 0$ are omitted for $y > y_{max}$.

corrected for sample-dependent γ-background and multiple scattering from sample plus container. In the latter case a simulated spectrum, containing single and multiple scattering,[31] is normalized to the area of the corresponding experimental spectrum; the simulated multiple scattering spectrum is then multiplied by the above normalization constant and subtracted from the experimental spectrum. An example of the comparison of experimental and simulated spectrum is reported in Fig. 2. As a final step, time of flight spectra are subsequently transformed to Neutron Compton profiles and normalized. A detailed description of the VESUVIO routines can be found in Refs. 22–25, 29, 30, and 31.

In order to derive the time of flight DINS proton signal heavy masses peaks have been fitted and then subtracted off. These peaks have been modeled using a sum of two Voigt functions, which satisfactorily reproduce the time of flight DINS signals from heavy atoms with Gaussian momentum distribution functions. Parameters of the Voigt line shapes have been refined, for each scattering angle, using a FORTRAN routine.[32] Time of flight DINS spectra, for each detector, have been expressed in terms of the scaling variable (or longitudinal momentum) $y = \frac{M}{q}(\omega - \frac{\hbar q^2}{2M})$, where $M = 1.0079$ amu, is the proton mass, using the following equation:[25]

$$F_l(y, q) = \frac{BM}{E_0 \Phi(E_0)} q C_l(t), \qquad (4)$$

where $F_l(y, q)$ is the fixed-angle experimental Compton profile for the lth detector, E_0 is the incident neutron energy, $\Phi(E_0)$ is the incident neutron spectrum, $C_l(t)$ is the count-rate at the lth detector, and B is a constant taking into account the detector solid angle, the detector efficiency at $E = E_1$, the time-energy Jacobian, the free-atom neutron proton cross section, the number of protons hit by the neutron beam.[3]

Fixed-angle histograms of $F_l(y, q)$ have been binned in the range $-30 \text{ Å}^{-1} \leq y \leq 30 \text{ Å}^{-1}$, with a bin width of 0.3 Å^{-1}. In the case of scattering angles above about 50° due to kinematics the upper limit of y, y_{max}, is lower than 30 Å^{-1} corresponding to upper values[33] of $q \simeq 600 \text{ Å}^{-1}$. For $y > y_{max}$, we set $F_l(y, q) = 0$, with an associate error of 10^4, i.e., approximately a factor of 2×10^6 larger than the average magnitude of the experimental error bars on the $F_l(y, q)$ spectra. This is carried out in order to obtain the same range and bin width for all data in the -30 Å^{-1} to 30 Å^{-1} range. This procedure guarantees that in the subsequent line shape analysis these artificially added points (with zero value, $F_l(y, q) = 0$) carry a negligible weight in the fitting.

The experimental $F_l(y, q)$ have been normalized to unit area, following the zero-order sum rule for the dynamical incoherent structure factor.[34] An example of normalized spectra is shown in Fig. 3: error bars of the experimental Compton profiles are of comparable magnitudes at high $|y|$, being slightly larger on the positive side. As discussed previously for high positive y values, data are more affected by noise at short time of flights. Figure 4 shows how the different $F_l(y, q)$ functions scale to collapse into a single detector averaged Compton profile.

B. Data analysis

The experimental Compton profiles and the $\bar{F}(y)$ were analyzed to determine the line shape of the momentum distribution, $\langle E_K \rangle$, and the mean force, respectively. This has been accomplished through two non-parametric and two parametric methods which rely on the following representation of $F_l(y, q)$, namely:[3]

$$F_l(y, q) = [J_{IA}(y) + \Delta J_l(y, q)] \otimes R_l(y, q), \qquad (5)$$
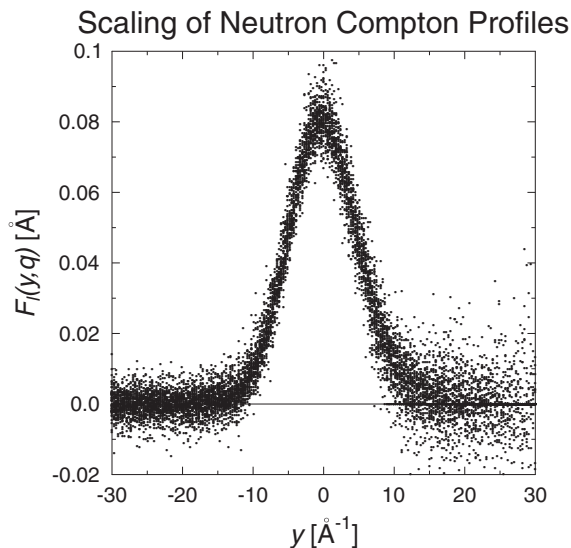
Scaling of Neutron Compton Profiles

FIG. 4. $F_l(y, q)$ (markers with omitted error bars) from all detectors. The plot shows the collapse of the profiles at different angles, demonstrating that the scattering regime reached in the present experiment is well described within the IA. For the highest angles, the artificially imposed $F_l(y, q) = 0$ are omitted for $y > y_{max}$.

FIG. 5. Experimental Neutron Compton Profile for ice at T = 271 K averaged over the whole set of the scattering angles ($\bar{F}(y) = <F_l(y, q) >_l$) (blue dots with error bars). The angle-averaged best fit is reported as a black continuous line for the M1 model. If final-state effects are not accounted for, the corresponding angle-averaged best fit is reported as a red dashed line (see text for details). The fits' residuals are also reported.

where $J_{IA}(y)$ is the longitudinal momentum distribution, $\Delta J_l(y, q)$ are the q-dependent deviations from the IA (final state effects), and $R_l(y, q)$ is the fixed-angle instrumental resolution function $R_l(y, q)$. The $R_l(y, q)$ functions have been determined using a standard procedure successfully employed for DINS experiments in a variety of systems:[35] the modified DINSMS Monte Carlo code[31] has been used to simulate the scattering of a polycrystalline Pb sample, which is currently used as a resolution calibration standard on VESUVIO.[25] DINS scattering from lead is dominated by the spectrometer's resolution, therefore a comparison between simulated and measured scattering from Pb provides an assessment of the reliability of the code to describe the spectrometer's response. A simulation of DINS scattering spectra in the IA is carried out for a fictitious sample with mass = 1.0079 amu and momentum distribution width $\sigma = 0.001$ Å^{-1}, i.e., assuming a scattering sample with infinitely narrow momentum distribution. The latter provides time of flight simulations of the spectrometer's response. The spectra are then transformed in proton's momentum space to obtain $R_l(y, q)$ for each lth detector.

The angle-averaged $F_l(y, q)$, $\bar{F}(y)$, is derived by calculating a simple average over the different detectors. This quantity, shown in Fig. 5, provides a graphical representation of the overall quality of the data. The $J_{IA}(y)$ line shape as well as $n(p)$ and $\langle E_K \rangle$ are calculated from the $F_l(y, q)$ spectra as follows: The $\langle E_K \rangle$ value is obtained by numerical integration of $\bar{F}(y)y^2$; a full analysis of the DINS line shape via simultaneous fitting of the individual $F_l(y, q)$ spectra with (a) a model-independent line shape, and (b) a three dimensional anisotropic Gaussian line shape derived from a quasi-harmonic model as suggested by a recent analysis of the PICPMD simulations for hexagonal ice.[12] As outlined in Ref. 36, the numerical integration of $\bar{F}(y)y^2$ provides a first-order estimate of σ^2 and $\langle E_K \rangle$, by subtracting the variance of
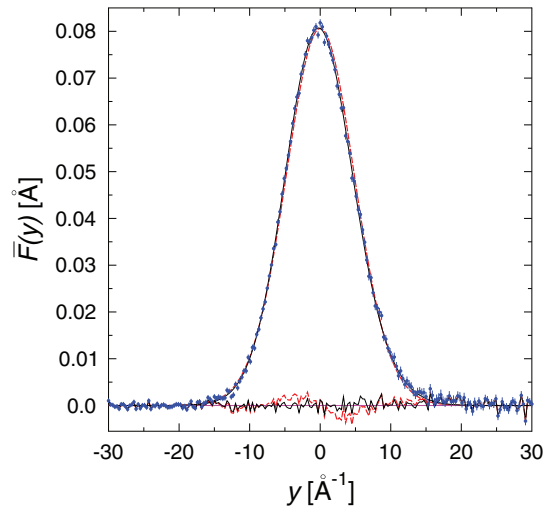
the angle-averaged resolution ($\sigma_R^2 = 0.98$ Å^{-2}), yelding $\sigma^2 = 27.0 \pm 2.7$ Å^{-2}. Systematic uncertainties, due to the limited range of integration, and residual differences between angle-averaged and constant-q representations of $\bar{F}(y)$ (Ref. 33) are evaluated to be $\simeq 0.3$ Å^{-2}. Therefore $\sigma = 5.2 \pm 0.3$ Å^{-1}, and $\langle E_K \rangle = 169 \pm 19$ meV. This can be used as a constraint for σ in fitting the $F_l(y, q)$ data set.

In the following, non-parametric methods of analysis of $\bar{F}(y)$ will be used to derive $\langle E_K \rangle$, from direct integration of the second central moment of $\bar{F}(y)$, or from the mean force $f(x)$.

The two parametric methods of analysis involved the fitting of the $F_l(y, q)$ spectra with either model-independent functions or multivariate Gaussians corresponding to a quasi-harmonic picture of the effective proton potential. The two methods, which we call M1 and M2, respectively, correspond to two different fitting procedures not available on the instrument program suite. For M1, the model-independent form for $J_{IA}(y)$ is[3,34]

$$J_{IA}(y) = \frac{e^{\frac{-y^2}{2\sigma^2}}}{\sqrt{2\pi}\sigma} \left[1 + \sum_{n=2}^{\infty} \frac{a_n}{2^{2n}n!} H_{2n}\left(\frac{y}{\sqrt{2}\sigma} \right) \right], \quad (6)$$

where H_{2n} are the Hermite polynomials and a_n the corresponding coefficients. The $n(p)$ is expressed in terms of a Gaussian times a series of Laguerre polynomials, $L_n^{1/2}(\frac{p^2}{2\sigma^2})$, with coefficients $(-1)^n a_n$. Equation (6) has the most general form, but may not facilitate interpretation of the data as it does not allow one to separate the effects of anharmonicity from those of anisotropy. In particular, in the case of ice, PICPMD simulations show that, within statistical errors, the momentum distribution of each individual proton is well approximated by a multivariate gaussian distribution with three distinct frequencies $\omega_{x,y,z}$. These are associated to local principal axes that depend on the crystalline orientation of the molecule to which the proton belongs.[12] This constitutes an anisotropic quasi-harmonic model in which the main effects of

anharmonicity are subsumed in the effective frequencies ω_i. Experiments access the total momentum distribution, i.e., the superposition of the distributions of all the protons in the sample. In polycrystalline samples a spherically averaged distribution originates in this way

$$n(p) = \left\langle \frac{1}{\sqrt{8\pi^3}\sigma_z\sigma_x\sigma_y} \exp\left(-\frac{p_z^2}{2\sigma_z^2} - \frac{p_x^2}{2\sigma_x^2} - \frac{p_y^2}{2\sigma_y^2}\right)\right\rangle_\Omega.$$
(7)

Here $\langle...\rangle_\Omega$ denotes spherical average and the variances $\sigma_{i=x,y,z}^2$ are related to the principal frequencies by $\sigma_i^2 = M\hbar\omega_i/2 \coth \beta\hbar\omega_i/2$. The ω_i frequencies are not directly reflected in Eq. (6). From PICPMD one obtains: $\omega_z = 2639 \pm 60$ cm^{-1}, $\omega_x = 1164 \pm 25$ cm^{-1}, $\omega_y = 775 \pm 20$ cm^{-1}.[12] There is a clear connection between these frequencies and the vibrational spectrum of ice. The latter includes four main features: a stretching band centered at $\approx$3200 cm^{-1}, a bending band centered at $\approx$1650 cm^{-1}, a broad libration band centered at $\approx$900 cm^{-1}, and a band of network modes below $\approx$400 cm^{-1}.[37] Careful analysis of the PICPMD data shows that ω_z, ω_y, and ω_x consist mainly of weighted averages of stretching, librational, and a mix of bending and librational frequencies, respectively, with redshifts due to additional network mode contributions and softening caused by anharmonicity.[12] The PICPMD simulations suggest that we should use Eq. (7) to fit the experimental distribution. In this model, labeled M2, σ_x, σ_y, and σ_z are treated as free parameters.

For finite q, the deviation from the IA can be accounted for by adding corrections,[3] to first order in $1/q$. In both M1 and M2 the underlying model for $\Delta J_l(y, q)$ is based on the original framework proposed by Sears.[34]

For finite q the experimental Compton profile is q-dependent and the following approximation is used:

$$J(y, q) = \left(1 - A_3(q)\frac{\partial^3}{\partial y^3}\right) J_{IA}(y) = J(y) + \Delta J(y, q).$$
(8)

Here the leading form of $J_{IA}(y)$ is assumed to have a simple Gaussian shape, and introducing $x = \frac{y}{\sqrt{2}\sigma}$ we have

$$-\frac{\partial^3}{\partial y^3}J_{IA}(y) = J_{IA}(y)\frac{1}{\sigma^3 2^{3/2}} H_3\left(\frac{y}{\sqrt{2}\sigma}\right),$$
(9)

where $H_3(x) = 8x^3 - 12x$. Since $A_3(q) = \frac{m\nabla^2 V}{36\hbar^2 q}$ we obtain, for an isotropic harmonic potential

$$\Delta J(y, q) = \frac{e^{\frac{-y^2}{2\sigma^2}}}{\sqrt{2\pi}\sigma} \frac{M^2\omega^2}{12\hbar^2 q} \frac{1}{\sigma^3 2^{3/2}} H_3\left(\frac{y}{\sqrt{2}\sigma}\right).$$
(10)

The q-independent factor, $\frac{M^2\omega^2}{12\hbar^2} \frac{1}{\sigma^3 2^{3/2}}$, in $\Delta J(y, q)$ defines a positive parameter, $c1$

$$\Delta J(y, q) = \frac{e^{\frac{-y^2}{2\sigma^2}}}{\sqrt{2\pi}\sigma} \frac{c1}{q} H_3\left(\frac{y}{\sqrt{2}\sigma}\right).$$
(11)

This term is asymmetric and induces a modulation in $J_{IA}(y)$. The dependence on q and on the scattering angle can be appreciated in Fig. 3, where the apparent centroid of $F_l(y, q)$ at the
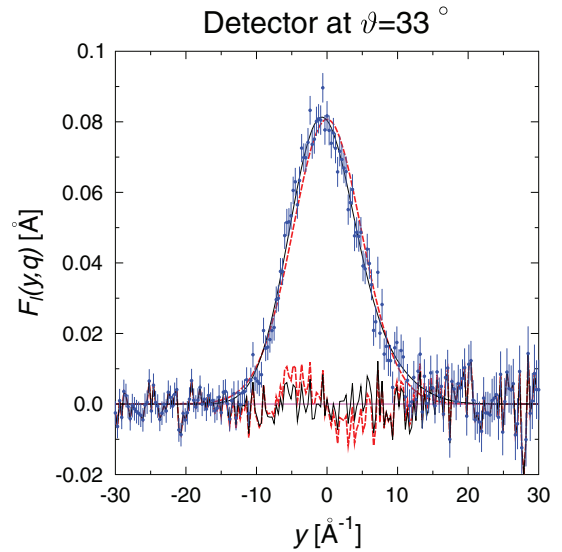

FIG. 6. Experimental Neutron Compton Profile, $F_l(y, q)$, at a scattering angle $\vartheta = 33°$ for ice at T = 271 K (blue dots with error bars). The best fit using M1 with the inclusion of FSE is reported as a black continuous line, while if FSE are not included in M1 the best fit is shown as a red dashed line. The fits' residuals are also reported.

lowest scattering angle is shifted to slightly negative y values, as well as in Fig. 5, where the average over all detectors shows the "average" shift of the centroids due the FSE.[34] Neglect of final state effects results in poorer fits with larger residuals, with typical asymmetric shape. In addition, if the final-state effects are not accounted for in the fitting, the kinetic energy derived, for example from M1, is reduced by approximately 5 meV. Figure 6 shows the modulation induced by FSE on a low angle detector spectrum.

Both M1 and M2 procedures rely on the minimization of

$$\chi^2 = \Sigma_l \Sigma_i \frac{\left(F_l^{th}(y_i, q_i) - F_l(y_i, q_i)\right)^2}{\epsilon_{l,i}^2},$$
(12)

where $F_l^{th}(y_i, q_i) = [J_{IA}(y_i) + \Delta J_l(y_i, q_i)] \otimes R_l(y_i, q_i)$. Here $J_{IA}(y_i) + \Delta J_l(y_i, q_i)$ is described by either M1 or M2 line shapes, the index l represents the detector index, the index i represent the y value at the ith bin, and $\epsilon_{l,i}^2$ is the error for each data point. The double sum over l and over i reflects the relevant properties:

$J_{IA}(y)$ is unique for all detectors; $\Delta J_l(y, q)$ varies across detectors due to the different q values accessed,[33] but $c1$ is independent of q and is unique for all detectors; $R_l(y, q)$ varies across detectors, but is a known function from the calibration procedures.

Based on the above physical assumptions, we have carried out the fitting, using M1 and M2, minimizing the above global chi square for all detectors simultaneously, to provide unique values (detector-independent) of σ, a_2, $c1$, σ_x, σ_y, σ_z. We consider the global fitting to be preferred to the fitting of individual detectors. The latter is generally used on VESUVIO to extract σ_l, a_{2l}, $c1_l$, etc., whose averages give the parameters σ, a_2, $c1$, ... However, the global fit has its basis on the invariance of $J_{IA}(y)$ and $c1$ across different detectors, while the individual fitting follows the approach of
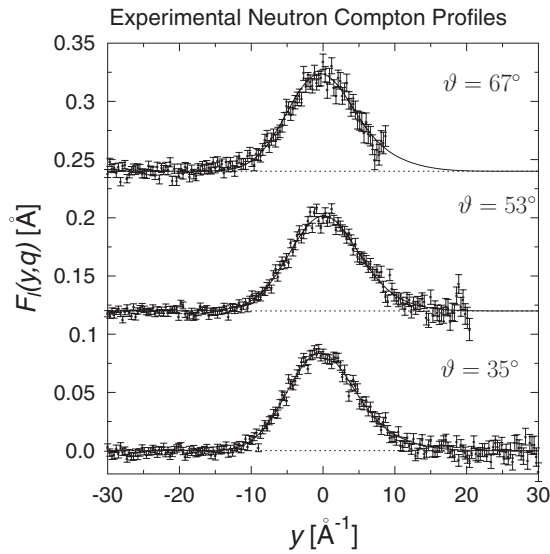
FIG. 7. $F_l(y, q)$ (markers with error bars), for three scattering angles, together with best fits using M1. Two of the spectra are shifted upwards for clarity. For the two highest angles, the artificially imposed $F_l(y, q) = 0$ are omitted for $y > y_{max}$.

finding l "statistically independent" momentum distributions to be subsequently averaged. However it has to be stressed that, since the chi square for individual detectors is weighted by the error bar, and the latter is poorly correlated with the noise present at high positive y, the results from individual detectors may be affected by the noise, since the latter is not accounted for by the chi square. On the other hand the global fitting provides a more efficient way for noise cancellation. The fit with the M1 model has been carried out using a FORTRAN code which makes use of the MINUIT chi square minimization routine,[32] while the fit with the M2 model has been carried out using a MATLAB code. Examples of the quality of fits for the M1 model are reported in Fig. 7.

The fit carried out using M1, yielded $\sigma = 4.99 \pm 0.03$ Å^{-1}, $a_2 = 0.10 \pm 0.01$ and $a_{n>2} = 0$, $c1 = 0.36 \pm 0.02$ and $\langle E_K \rangle = 156 \pm 2$ meV.

In the case of the spherically averaged multivariate Gaussian, M2, there is, however, a difficulty, since optimization gives nearly degenerate σ_x and σ_y values leaving the error bars on the effective frequencies poorly defined. This reflects the presence of one too many fitting parameters for the information content of the (spherically averaged) data set. Indeed the difficulty would disappear by adopting a model with only two distinct parameters (σ_z and $\sigma_t = \sigma_x = \sigma_y$ in the transverse direction) as done in a previous study,[8] but this would not be an accurate representation of the physics. Rather than following this approach, in the M2 model we retain three distinct σ_i and eliminate the degeneracy by adding a weighting term in the least square fit of the experimental Compton profiles, to minimize the deviation of the fitted σ_i from their PICPMD counterparts (see below for details). The magnitude of the weighting term reflects the assumed physical ranges for the σ_i or, equivalently, the ω_i.

If $\sigma_x^2, \sigma_y^2, \sigma_z^2$ are treated as unconstrained free parameters, minimizing χ^2 in Eq. (12) yields, given the accuracy of

the current data, nearly degenerate σ_x and σ_y. However, σ_x and σ_y should be distinct from each other, as they reflect distinct averaged information on the bending and the libration frequencies of the vibrational spectrum. Such anisotropic behavior in the spherical momentum distribution is largely suppressed by the spherical averaging operation. Thus to obtain distinct σ_x and σ_y values from the spherically averaged momentum distribution, a significantly higher resolution would be needed than currently available with state-of-the-art facilities and instrumentation. While it should be possible to achieve the required resolution in the future, at present the only way to acquire directional information from experiments on macroscopically isotropic samples such as polycrystalline ice, is to use prior knowledge on the distribution in the fitting procedure. In this respect, PICPMD simulations are a reliable source of theoretical knowledge, since (i) they predict momentum distributions in good agreement with experiment and (ii) they are a parameter-free approach in which the only physical approximation is associated to the adopted electronic density functional.

As shown in Ref. 12, the PICPMD data for the momentum distribution are accurately reproduced by a quasi-harmonic model with principal frequencies $\omega_z^{PI} = 2639 \pm 60$ cm^{-1}, $\omega_x^{PI} = 1164 \pm 25$ cm^{-1}, $\omega_y^{PI} = 775 \pm 20$ cm^{-1}. In the M2 model, $\sigma_x^2, \sigma_y^2, \sigma_z^2$ are used as fitting variables. From the relation

$$\sigma_i^2 = \frac{M\hbar\omega_i}{2} \coth \frac{\beta\hbar\omega_i}{2},\qquad(13)$$

the PICPMD principal frequencies correspond to $(\sigma_x^2)^{PI} = 39.4$ Å^{-2}, $(\sigma_y^2)^{PI} = 17.5$Å^{-2}, $(\sigma_z^2)^{PI} = 12.0$Å^{-2}. Assuming that the deviation of the actual σ_k^2 from $(\sigma_k^2)^{PI}$ follows a Gaussian probability distribution with standard deviation $\Delta\sigma_i^2$, one has

$$P(\sigma_k^2) \propto e^{-\frac{[\sigma_k^2 - (\sigma_k^2)^{PI}]^2}{2(\Delta\sigma_k^2)^2}}.\qquad(14)$$

$\Delta\sigma_i^2$ reflects the uncertainty of σ_i^2, which depends on the likelihood interval suggested by physics and the experimental resolution. In our fit we take $\Delta\sigma_x^2 = 1.5$, $\Delta\sigma_y^2 = 1.2$, $\Delta\sigma_z^2 = 3.0$. These values correspond to the following 70% confidence intervals for the principal frequencies ω_k:

$$\omega_x \in [1059, 1265]\text{cm}^{-1}, \quad \omega_y \in [681, 861]\text{cm}^{-1},$$

$$\omega_z \in [2430, 2830]\text{cm}^{-1}.\qquad(15)$$

The assumed distribution for σ_k^2 (14) is used as *prior* information in the maximum likelihood method,[38] yielding a modified objective function to be minimized

$$\chi^2(\sigma_x^2, \sigma_y^2, \sigma_z^2) = \Sigma_l \Sigma_i \frac{\left(F_l^{th}(y_i, q_i) - F_l(y_i, q_i)\right)^2}{\epsilon_{l,i}^2}$$

$$+ \sum_{k=x,y,z} \frac{\left[\sigma_k^2 - (\sigma_k^2)^{PI}\right]^2}{2(\Delta\sigma_k^2)^2}.\qquad(16)$$

We obtain in this way $\omega_z = 2797 \pm 95$ cm^{-1}, $\omega_x = 1233 \pm 110$ cm^{-1}, $\omega_y = 922 \pm 81$ cm^{-1}, where the relatively large error bars reflect the estimates for the physical range made in the fit.
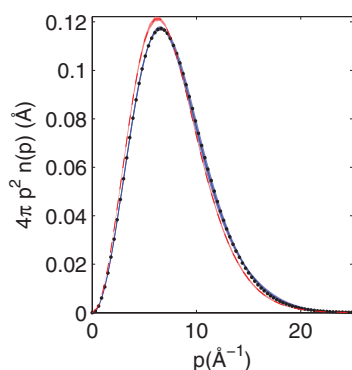
FIG. 8. Experimental radial momentum distribution for ice at 271 K obtained using model M1 (blue solid line), M2 (black dots) and PICPMD for ice at 269 K (red dashed line) with error bars. Errors on the radial momentum distribution, for both M1 and M2, are very small : they are determined from the parameters' covariance matrix calculated by the fitting codes.
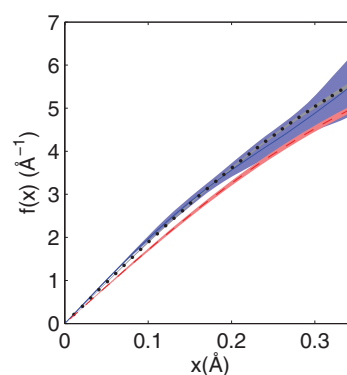

FIG. 9. Mean force, with error bars, calculated directly from the experimental asymptotic Compton profile, $\bar{J}_{IA}(y)$ (blue solid line), M2 (black dots), and PICPMD data (red dashed line).

III. DISCUSSION AND CONCLUSIONS

The two parametric methods, M1 and M2, yielded the experimental proton momentum distribution of ice. In Fig. 8 we report the radial momentum distributions, $4\pi p^2 n(p)$, from M1, M2 and PICPMD, respectively. The M2 model fits the experimental data just as well as the M1 model, confirming that the added bias does not worsen in any way the quality of the fit. The blueshifts of the "experimental" frequencies relative to their PICPMD counterparts suggest that the experimental $n(p)$ should be slightly more spread out than its theoretical counterpart, an outcome that is entirely borne out by the plot of the PICPMD radial distribution reported in Fig. 8.

Interestingly, the comparison between PICPMD and the present more accurate experiment reverses the trend observed in the comparison with the previous experiment of Ref. 8: the proton is now more localized in the experiment than in the calculation, consistent with the delocalization error of common density functional theory approximations.[9] The effect can be quantified in terms of $\langle E_K \rangle$, which is 156 ± 2 meV with the M1 fit and 154 ± 2 meV with the M2 fit, as opposed to 143 ± 2 meV in PICPMD. The relative insensitivity of the spherical momentum distribution to the anisotropy of a system characterized by three distinct quasi-harmonic frequencies confirms a recent theoretical study,[39] in which a more sensitive quantity named mean force was proposed. For a macroscopically isotropic system, the latter is a function of the radial displacement x. The mean force is $f(x) = (-\log n(x))' - \frac{Mx}{\beta \hbar^2}$. Here $n(x)$ is the spherical end-to-end distribution, i.e., the Fourier transform of $n(p)$ (Eq. (7)), while the second term is the free particle contribution which is independent of the environment; $f(x)$ can be directly related to the experimental $\bar{J}_{IA}(y)$ data obtained after correcting the NCP data $\bar{F}(y)$ for final state effects $\Delta J(y, q)$. The corresponding expression is[39]

$$f(x) = -\frac{Mx}{\beta \hbar^2} + \frac{\int_0^\infty dy \ y \sin(xy/\hbar) \bar{J}_{IA}(y)}{\hbar \int_0^\infty dy \ \cos(xy/\hbar) \bar{J}_{IA}(y)}. \qquad (17)$$

The mean forces extracted from $J_{IA}(y)$ Eq. (17), from M2, and from PICPMD data are plotted in Fig. 9. The three mean forces have good correspondence, and $f(x)$ extracted from the "raw" experimental data is particularly close to that of the M2 model, indicating that the quantum state of the proton in ice is well represented by quasi-harmonic anisotropic motion. Notice that the error bars of $f(x)$ increase systematically with the displacement x, reflecting a progressively larger statistical uncertainty as the tail of the end-to-end distribution is approached; $f(x)$ is related to the derivative of the Fourier transform of the NCP, and therefore, at large x, becomes sensitive to its highest frequency components, i.e., to the noise. The effect becomes so pronounced in the "raw" $f(x)$ that we truncate the plot at 0.35 Å. The $\langle E_K \rangle$ estimated, in a fourth, non parametric way, from the "raw" $f(x)$ is 156 ± 9 meV. The error bar of this estimate is larger than that from M1 or M2, since the "raw" mean force constitutes a model independent, non-parametric approach. To accurately resolve the anisotropic frequencies without resorting to a model dependent approach, the counting statistics in the experiment, i.e., the uncertainty of the "raw" $f(x)$ should be comparable to that of the M2 model in Fig. 9. This work illustrates how the theoretical and experimental determination of the momentum distribution in a benchmark system like polycrystalline ice can directly access the physical mechanisms describing the proton quantum state. We have successfully extracted the dominant features of the microscopic directional momentum distribution from an experiment on a macroscopically isotropic sample. Moreover, we have measured with high precision the non-trivial quantum excess kinetic energy, an observable that can be used as a quantitative benchmark for electronic density functionals employed in the description of hydrogen bonded systems in "*ab initio*" numerical simulations. An accurate measurement of the kinetic energy is in fact the most direct experimental probe of the localization/delocalization of the proton, and can contribute to the development of better theoretical descriptions of water and hydrogen bonded systems in general. This study can be further used to investigate the role of nuclear quantum effects in a variety of hydrogen bonded systems.

ACKNOWLEDGMENTS

[1] *Hydration Processes in Biology: Theoretical and Experimental Approaches*, NATO ASI Series A: Life Sciences Vol. 305, edited by M. C. Bellisent Funel (IOS, Amsterdam, 1998).

[2] P. G. Debenedetti, *Metastable Liquids: Concepts and Principles* (Princeton University Press, Princeton, 1997); G. W. Robinson, S.-B. Zhu, S. Singh, and M. W. Evans, *Water in Biology, Chemistry and Physics* (World Scientific, Singapore, 1999).

[3] C. Andreani, D. Colognesi, J. Mayers, G. F. Reiter, and R. Senesi, Adv. Phys. **54**, 377 (2005).

[4] R. Senesi, C. Andreani, Z. Bowden, D. Colognesi, E. Degiorgi, A. L. Fielding, J. Mayers, M. Nardone, J. Norris, M. Praitano, N. J. Rhodes, W. G. Stirling, J. Tomkinson, and C. Uden, Physica B **276–278**, S189 (2000).

[5] G. F. Reiter, J. Mayers, and J. Noreland, Phys. Rev. B **65**, 104305 (2002).

[6] G. F. Reiter, J. Mayers, and P. Platzman, Phys. Rev. Lett. **89**, 135505 (2002).

[7] C. Pantalei, A. Pietropaolo, R. Senesi, C. Andreani, S. Imberti, J. Mayers, C. J. Burnham, and G. F. Reiter, Phys. Rev. Lett. **100**, 177801 (2008).

[8] G. Reiter, J. C. Li, J. Mayers, T. Abdul-Redah, and P. Platzman, Braz. J. Phys. **34**, 142 (2004).

[9] A. J. Cohen, P. Mori-Sanchez, and W. Yang, Science **321**, 792 (2008).

[10] R. Moreh and D. Nemirovski, J. Chem. Phys. **133**, 084506 (2010).

[11] C. Andreani, E. Degiorgi, R. Senesi, F. Cilloco, D. Colognesi, J. Mayers, M. Nardone, and E. Pace, J. Chem. Phys. **114**, 387 (2001).

[12] L. Lin, J. A. Morrone, R. Car, and M. Parrinello, Phys. Rev. B **83**, 220302(R) (2011).

[13] A. Pietropaolo, R. Senesi, C. Andreani, A. Botti, M. A. Ricci, and F. Bruni, Phys. Rev. Lett. **100**, 127802 (2008).

[14] A. Pietropaolo, R. Senesi, C. Andreani, and J. Mayers, Braz. J. Phys. **39**, 318 (2009).

[15] V. Garbuio, C. Andreani, S. Imberti, A. Pietropaolo, G. F. Reiter, R. Senesi, and M. A. Ricci, J. Chem. Phys. **127**(15), 154501 (2007).

[16] R. Senesi, A. Pietropaolo, A. Bocedi, S. E. Pagnotta, and F. Bruni, Phys. Rev. Lett. **98**, 138102 (2007).

[17] G. Reiter, R. Senesi, and J. Mayers, Phys. Rev. Lett. **105**, 148101 (2010).

[18] C. Pantalei, R. Senesi, C. Andreani, P. Sozzani, A. Comotti, S. Bracco, M. Beretta, P. E. Sokol, and G. Reiter, Phys. Chem. Chem. Phys. **13**, 6022 (2011).

[19] J. A. Morrone and R. Car, Phys.Rev. Lett. **101**, 017801 (2008).

[20] R. Car and M. Parrinello, Phys. Rev. Lett. **55**, 2471 (1985).

[21] D. Marx and M. Parrinello, Z. Phys. B **95**, 143 (1994); J. Chem. Phys. **104**, 4077 (1996).

[22] A. Pietropaolo, C. Andreani, A. Filabozzi, E. Pace, and R. Senesi, Nucl. Instrum. Methods Phys. Res. A **570**, 498 (2007).

[23] M. Tardocchi, A. Pietropaolo, C. Andreani, A. Bracco, A. DAngelo, G. Gorini, S. Imberti, N. J. Rhodes, R. Senesi, and E. M. Schooneveld, Nucl. Instrum. Methods Phys. Res. A **526**, 477 (2004).

[24] M. Tardocchi, A. Pietropaolo, C. Andreani, G. Gorini, N. Rhodes, E. M. Schooneveld, and R. Senesi, Rev. Sci. Instrum. **75**, 4880 (2004).

[25] J. Mayers, Meas. Sci. Technol. **22**, 015903 (2011).

[26] G. B. West, Phys. Rep. **18C**, 263 (1975).

[27] C. Andreani, G. Gorini, E. Perelli-Cippo, A. Pietropaolo, N. Rhodes, E. M. Schooneveld, R. Senesi, and M. Tardocchi, Appl. Phys. Lett. **85**, 5454 (2004).

[28] A. Pietropaolo, M. Tardocchi, E. M. Schooneveld, and R. Senesi, Nucl. Instrum. Methods Phys. Res. A **568**, 826 (2006).

[29] E. M. Schooneveld, A. Pietropaolo, C. Andreani, G. Gorini, J. Mayers, N. J. Rhodes, R. Senesi, and M. Tardocchi, Rev. Sci. Instrum. **77**, 095103 (2006).

[30] C. Andreani, A. Pietropaolo, R. Senesi, G. Gorini, M. Tardocchi, A. Bracco, N. J. Rhodes, and E. M. Schooneveld, Nucl. Instrum. Methods Phys. Res. A **481**, 509 (2002).

[31] J. Mayers, A. L. Fielding, and R. Senesi, Nucl. Instrum. Methods Phys. Res. A **481**, 454 (2002).

[32] F. James, MINUIT Minimization Package, Reference Manual CERN Program Library, Geneva, 1994.

[33] R. Senesi, A. Pietropaolo, and C. Andreani, Nucl. Instrum. Methods Phys. Res. A **594**, 244 (2008).

[34] V. F. Sears, Phys. Rev. B **30**, 44 (1984).

[35] C. Andreani, C. Pantalei, and R. Senesi, Phys. Rev. B **75**, 064515 (2007).

[36] T. R. Sosnick, W. M. Snow, and P. E. Sokol, Phys. Rev. B **41**, 11185 (1990).

[37] D. S. Eisenberg and W. Kauzmann, *The Structure and Properties of Water* (Clarendon, Oxford, 1969).

[38] D. Ruppert, *Statistics and Data Analysis for Financial Engineering* (Springer Science, New York, 2010).

[39] L. Lin, J. A. Morrone, R. Car, and M. Parrinello, Phys. Rev. Lett. **105**, 110602 (2010).